



Experimental study of eddy viscosity for breaking waves on sloping bottom and comparisons with empirical and numerical predictions

Nelly Oldekop^{a*}, Toomas Liiv^b, and Janek Laanearu^a

^a Department of Civil Engineering and Architecture, School of Engineering, Tallinn University of Technology, Ehitajate tee 5, 19086 Tallinn, Estonia

^b Corson LLC, Laki 14a-704, 10621 Tallinn, Estonia

Received 8 February 2019, accepted 6 May 2019, available online 30 June 2019

© 2019 Authors. This is an Open Access article distributed under the terms and conditions of the Creative Commons Attribution-NonCommercial 4.0 International License (<http://creativecommons.org/licenses/by-nc/4.0/>).

Abstract. Focus is on the turbulence for a plunging breaker. Laser Doppler anemometer point measurements were used to determine the velocity matrix of a breaking wave on a sloping bottom. Using the Reynolds stress anisotropy for incompressible fluid, it was found that the ensemble averaged measured velocity predicted eddy viscosity is associated with peaks, which are absent in the broadly accepted empirical predictions. The instantaneous eddy viscosity coefficient was determined according to the Reynolds stresses, modified mean velocity and its gradient components and turbulent kinetic energy. The modified mean velocity and its derivatives improve eddy viscosity predictions during the wave period, which gives evidence that the velocity used corresponds well to a rotational part. In addition to the measurement predictions, empirical formulae were used to estimate the eddy viscosity values during the wave period. Furthermore, a meshless numerical model is proposed to determine artificial viscosity and demonstrate its dependence on eddy viscosity in the case of weakly compressible fluid.

Key words: artificial viscosity, breaking wave, eddy viscosity, experiment, turbulence.

1. INTRODUCTION

In the process of nearshore wave breaking, the sloping bottom can be a solid body such as a rock or a set of small mobile particles as sediments. Wave breaking is of high significance in the coastal process, which is responsible for nearshore sediment transport and concurrent development of bed forms. The knowledge of wave breaking is needed to solve a number of the coastal engineering problems associated with the bottom changes, pollution propagation and wave forces on coastal structures. The bottom and surface boundary layers are treated in very different ways in the coastal engineering models. The turbulence is generated both in the surface and bottom boundary layers, which merge in the surf zone. The coastal environment represents a complex dynamical system, where waves and currents interact with bed forms (Laanearu et al., 2007). An ability to predict the geometrical characteristics of the bed forms in the coastal zone under wave action requires an accurate representation of the physics of the sediment transport processes. The effects of waves on morphodynamical changes depend on the wave's Reynolds number

* Corresponding author, nelly@corson.ee

and the frictional factor of the boundary layer (Madsen and Grant, 1976). To compliment previous works that are using empirical criteria by giving a more flexible and accurate description of the turbulence due to a breaking wave, the eddy viscosity profiles are needed for more accurate nearshore wave modelling (Briganti et al., 2004). The deformation of the wave profile in the surf zone is essentially due to the bottom shapes, whereas the surface waves approaching the coast lose their momentum in the attenuation related to the bottom stress, breaking of surface and concurrent reflection processes due to the run-up. Research progress on the breaking waves and the surf zone dynamics is reviewed by Peregrine (1983), Battjes (1988), and Svendsen and Putrevu (1996).

Detailed modelling of turbulence in breaking waves is a difficult task for a number of reasons; the velocity field during breaking is extremely chaotic and varies rapidly in space and time. Available models can handle most of wave phenomena, such as shoaling, refraction, diffraction, but prediction of the breaking event is challenging. Surface breaking is associated with the irreversible transformation of potential velocity field into motions of different types and scales, including the turbulence, vortices and air-water interactions. Therefore, in the coastal engineering studies, the meshless numerical modelling, such as Smoothed Particle Hydrodynamics (SPH) solvers, is becoming more useful (Monaghan, 1994). It has been demonstrated that the SPH models are suitable to reproduce free surface phenomena such as a breaking wave (Dalrymple and Rogers, 2006; Shao, 2006; De Padova et al., 2009), dam breaks (Gomez-Gesteira et al., 2010; Lee et al., 2010), whitewater formation (Morris, 2000), waves overtopping of harbour structures (Rogers et al., 2010), tsunamis generated landslide (Capone et al., 2010). However, the near-bottom velocity modelling is problematic in SPH, which may complicate solving practical coastal engineering problems.

Extensive experimental work on coastal hydrodynamics and sediment transport in the laboratories is targeted to understanding complicated dynamics involved in accurate field measurements. However, as the size of most wave flumes is fairly limited, it is difficult to obtain adequately large values of the Reynolds number for modelling boundary layer dynamics. Therefore, for a simplified experimental setup, a U-shaped oscillating tunnel (U-tube) is suggested by Lundgren and Sorensen (1958), where the orbital motion in the test section differs from the real wave induced flow by being entirely uniform in the along tube direction and by having no vertical orbital motion. In this study, the wall generated turbulence, as in the U-tube experiments, is complemented with the turbulence generated at free surface, which is absent in the U-tube oscillating flow. The U-shape oscillatory wave motion is an acceptable solution for modelling characteristics of the wave bottom boundary layer on a constant water depth with regular non-breaking waves. However, the method is lacking accuracy on the sloping bottom with breaking waves, where the free surface generated turbulence can extend into a full water column. Studies by Ting and Kirby (1994, 1995, and 1996), Chang and Liu (1999) and Liiv (2007) have reported laboratory measurements of velocities and turbulence intensities in periodic breaking waves. All of these measurements were recorded by a laser Doppler anemometer (LDA). The latest of these experiments reported by Liiv (2007) is revisited herein to make use of the novel unpublished experimental data.

Many empirical models are available to deal with the eddy viscosity for turbulence that is generated in the surf zone. Approximation of Reynolds stress anisotropy allows to determine the eddy viscosity as the product of functions of velocity and of distance. According to the mixing length model, the length is specified on the basis of the geometry of the flow. This is used in a number of wave modelling tools, e.g., MIKE21 FLOW MODEL HD (product of MIKE Powered by DHI). However, in the momentum transport models, such as two equation models, e.g., $k-\varepsilon$ model, velocity and length are related to the turbulent kinetic energy as well as to the rate at which energy is dissipated. Even in relatively simple flows, the eddy viscosity concept can fail due to regions inside of which the shear stress and the velocity gradient of the flow have opposite signs (Rodi, 1980).

The paper is organized as follows. In section 2, the physical model described by Oldekop and Liiv (2013) is revisited to address the experimental observations of the breaking waves and to describe the experimental setup and measurements. In the first subsection of the methodology part, a generalized mathematical formulae are proposed to predict the instantaneous eddy viscosity coefficient according to the Reynolds stresses, mean velocity gradient components and turbulent kinetic energy, which are measured during a number of wave periods. Also, this section presents the empirical formulae extensively

used in the coastal engineering modelling. In the second subsection of the methodology, the meshless numerical model is proposed to reproduce the wave breaking process on the sloping bottom of the shortened wave flume. In the results section, a novel eddy viscosity formulation with modified mean velocity and its derivatives is presented for the case of non-isotropic turbulence. In addition, the averaged eddy viscosity values are compared with the empirical and numerical predictions. In the discussion section, the field modifications of the mean velocity and its derivatives are explained. Finally, conclusions are outlined based on the overall results.

2. PHYSICAL MODEL

Experimental studies of breaking waves with the propagation of regular waves over a uniformly sloping bottom were carried out in the wave flume with a bottom slope of a constant 1 to 17 positioned in one end (Fig. 1). Wave flume itself was 0.6 m in width, 0.6 m in depth and 22 m in length (Fig. 1). The origin of the coordinate system was taken at the still water height 0.3 m, where the inclined bottom of the flume begins (see RP, standing for reference point in Fig. 1).

Waves were created using a flap-type wave generator situated at the other end of the wave flume from the slope (Fig. 1), which enables generation of regular waves. Wave generator divided the constant depth of the water body into a regular waves area and a ballast water area. Dumping of the wave generator backside waves was established inside of the ballast water area by using four layers of metal net with size of 3 mm by 3 mm and 50 mm step in between the layers. A computer was used to produce signals for making regular sinusoidal waves controlled by the generator. Velocity profiles were measured in the breaking waves using a two component Argon-ion laser Doppler anemometer (LDA) with an output power of 1.3 W (Fig. 1). The measuring system was based on a two-dimensional tracker that operated in forward scatter fringe mode. The two velocity components were measured simultaneously. The flow velocity data were collected with a sampling frequency of 1 kHz during 151 wave periods. During the signal drop-out caused by air bubbles blocking the laser beams, the frequency tracker kept the output voltage the same as the voltage just before the drop-out. To ensure signal dropping, the drop-out signal was recorded simultaneously with the output of regular channels. The synchronizing mechanism (Fig. 1) was made by a pair of electrodes and was positioned above the still water level in the constant depth section of the flume. Capacity probes in wave gauge were used to measure variations in wave height (Fig. 1). Table 1 shows the main characteristics of the regular wave in the experimental runs.

As the LDA system allows measurements at one point, the measurements were repeated over 29 profiles along the slope. The measuring step in the vertical direction was 1 mm in the near bed zone, 3 mm

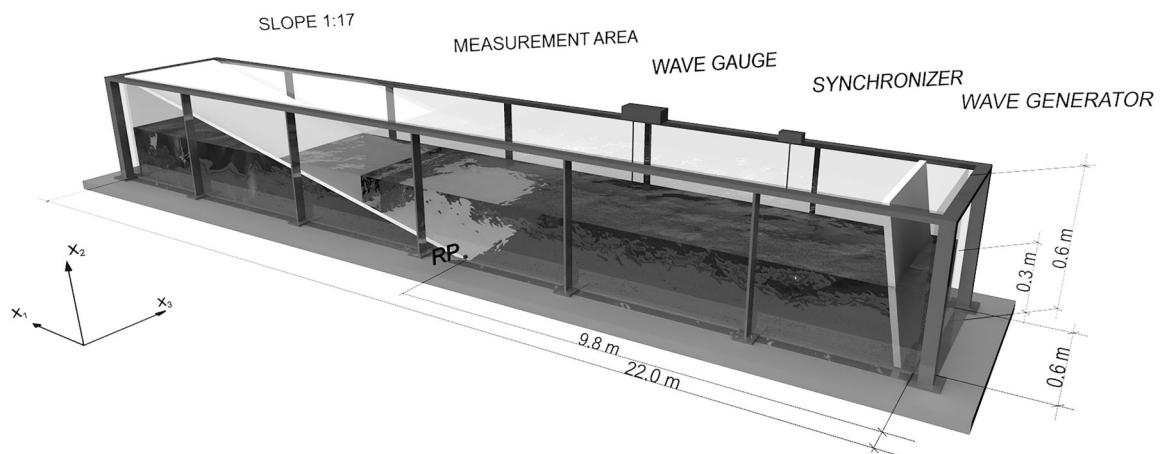


Fig. 1. Bird view of the wave flume: dimensions and notation.

Table 1. Regular wave characteristics

T , s	h_b , m	d_b , m	x_b , m	H_0 , m	L_0 , m	H_b , m	C_0 , m s ⁻²
2.03	0.106	0.111	2.90	0.072	6.0	0.118	1.72

Table 2. Location of measuring profiles and corresponding wave parameters

Profile No.	Distance from the reference point RP, m	Still water depth d , m	Water depth with wave set-up h , m	Wave celerity C , m s ⁻²
16	2.80	0.118	0.116	1.069
17	2.81	0.118	0.115	1.064
18	2.82	0.117	0.114	1.059

in the intermediate zone and 2 mm in the zone affected directly by the water surface motion. The closest measurement point to the bottom was 0.05 mm above the rigid bed of the slope. For this paper, three neighbouring profiles were chosen to analyse the velocity changes during the breaking waves. The parameters observed in the experimental runs are presented in Table 2.

During experimental runs, horizontal and vertical components, the corresponding signal drop-outs, water level variation and the signal from the synchronizing mechanism were stored. To determine ensemble averaged unsteady mean velocity and velocity fluctuation, data were collected for 151 waves.

The physical model of the wave flume and preliminary data processing of the experimental tests of breaking waves on the sloping bottom developed at Tallinn University of Technology (TalTech) is described in detail by Liiv (2007). Essentially, findings of previous investigations on the bottom boundary layer (Fredsoe, 1992) in U-shaped oscillating tunnels were compared with new experimentally observed results produced in the TalTech wave flume, and it was concluded that calculations of semi-logarithmic dimensionless velocity distributions were significantly different from those proposed previously. In addition, the two-dimensional ensemble averaged velocity components and turbulent kinetic energy fields are presented by Liiv and Lagemaa (2008). The study by Oldekop and Liiv (2013) found a considerable space and time variation in both bottom and wave boundary layers of the shear stress term in the surf zone. They conclude that the turbulence generated during the wave breaking has a strong effect on the shape of the shear velocity profiles. In the study by Oldekop and Liiv (2013), the measured velocity profiles before and after wave breaking are compared to demonstrate the effect of generated turbulence on the wave dynamics in the surf zone.

3. METHODOLOGY

In this section, the turbulence modelling is specified with eddy viscosity coefficients that can be explicitly or implicitly determined. In the case of the theoretical and empirical models, the eddy viscosity is determined by explicit mathematical formulae, and in the case of the numerical model, the eddy viscosity is determined by implicit numerical modelling.

3.1. Theoretical and empirical models

The Reynolds stresses can be used to determine the eddy viscosity at any point of the turbulent flow field. At each point and time, the Reynolds stress anisotropy $a_{ij} \equiv \langle u_i u_j \rangle - \frac{2}{3} k_T \delta_{ij}$, which corresponds to turbulent shear stresses, is determined by the mean velocity gradient $\nabla \langle U \rangle$ components and eddy viscosity ν_T . The corresponding Reynolds stresses for a compressible fluid are

$$\begin{aligned}
 -\langle u_i u_j \rangle &= -\frac{2}{3} k_T \delta_{ij} + \nu_T \left(\frac{\partial \langle U_i \rangle}{\partial x_j} + \frac{\partial \langle U_j \rangle}{\partial x_i} - \frac{2}{3} \frac{\partial \langle U_k \rangle}{\partial x_k} \delta_{ij} \right) = \\
 &= -\frac{2}{3} \left(k_T + \nu_T \frac{\partial \langle U_k \rangle}{\partial x_k} \right) \delta_{ij} + \nu_T \left(\frac{\partial \langle U_i \rangle}{\partial x_j} + \frac{\partial \langle U_j \rangle}{\partial x_i} \right),
 \end{aligned} \tag{1}$$

where k_T is the turbulent kinetic energy, δ_{ij} is the Kronecker delta and ν_T is the eddy viscosity. Reynolds stress is proportional to the mean rate of the compression and shear strain, where the positive scalar coefficient ν_T is the eddy viscosity. It is only the anisotropic component a_{ij} that is effective in transporting momentum, while the isotropic component $\frac{2}{3}k_T$ can be absorbed in a modified mean pressure. The total viscous stresses are given by augmenting the molecular viscosity with an eddy viscosity (see Bertin et al., 1992).

For the turbulent channel flows, symmetries in the flow geometry determine the properties of the Reynolds stresses. Considering a statistically two-dimensional flow in which statistics are independent of the cross-channel coordinate x_3 (see Fig. 1), the Reynolds stress tensor for a turbulent flow in the flume may be approximated as

$$\langle u_i u_j \rangle = \begin{bmatrix} \langle u_1^2 \rangle & \langle u_1 u_2 \rangle & 0 \\ \langle u_1 u_2 \rangle & \langle u_2^2 \rangle & 0 \\ 0 & 0 & \langle u_3^2 \rangle \end{bmatrix}, \tag{2}$$

which applies to the turbulent channel flow with an inclined bottom, i.e., with a slope in along-channel coordinate x_1 direction and vertical x_2 direction.

In a two-dimensional turbulent oscillatory flow, the instantaneous local velocity components (U_1 for the horizontal component, U_2 for the vertical component) may be decomposed into phase ensemble components ($\langle U_1 \rangle, \langle U_2 \rangle$) and turbulent components ($\langle u_1 \rangle, \langle u_2 \rangle$), e.g. $\vec{U} = \langle \vec{U} \rangle + \langle \vec{u} \rangle$. The vertically averaged (over three measurement points) variables are functions of time and distance, e.g.,

$$\langle U_i \rangle = \frac{1}{\Delta x_j} \int_{x_j}^{x_j + \Delta x_j} U_i dx_j. \tag{3}$$

Making use of the Reynolds stress anisotropy, Eq. (1) can be applied to derive a formula for the eddy viscosity coefficient that results from the non-diagonal elements, which in the present case takes the form

$$\nu_T = \frac{-\langle u_1 u_2 \rangle}{\frac{\partial \langle U_1 \rangle}{\partial x_2} + \frac{\partial \langle U_2 \rangle}{\partial x_1}}, \tag{4}$$

and from the diagonal elements, which in the present case takes the form

$$\nu_T = \frac{\frac{2}{3} k_T - \langle u_i u_i \rangle}{2 \frac{\partial \langle U_i \rangle}{\partial x_i} - \frac{2}{3} \left(\frac{\partial \langle U_1 \rangle}{\partial x_1} + \frac{\partial \langle U_2 \rangle}{\partial x_2} \right)}. \tag{5}$$

The turbulent kinetic energy $k_T = \frac{1}{2} (\langle u_1^2 \rangle + \langle u_2^2 \rangle + \langle u_3^2 \rangle)$ is approximated for the two-dimensional turbulent oscillatory flow as

$$k_T \approx \frac{1}{2} (\langle u_1^2 \rangle + \langle u_2^2 \rangle), \quad (6)$$

where the turbulent kinetic energy calculation is simplified due to conditions $\langle u_1 \rangle > \langle u_2 \rangle \gg \langle u_3 \rangle$.

Turbulent viscosity $\nu_T(x, t)$, can be expressed empirically as the product of a shear velocity $U^*(x, t)$ and a length scale $l^*(x, t)$:

$$\nu_T = U^* l^*. \quad (7)$$

Considering the mixing length model, l^* for Eq. (7) is specified on the basis of the geometry of the flow. In engineering-type modelling, eddy viscosity is usually specified in one of the four different ways: a) by omitting eddy terms; b) by giving constant value for each area; c) by a data file where each grid point has its defined value, or d) by dynamic calculations using Smagorinsky formula. Based on the second option (b), a uniform eddy term is chosen based on:

$$\nu_T = 0.02 \frac{\Delta x_1 \Delta x_2}{\Delta t}, \quad (8)$$

where $\Delta x_1 \Delta x_2$ is the grid spacing $90 \times 3 \text{ mm}^2$ and Δt is the time step 1/1000 s.

However, calculations based on the fourth option (d), the Smagorinsky formula

$$\nu_T = C_S^2 \Delta x_1 \Delta x_2 \sqrt{\left(\frac{\partial \langle U_i \rangle}{\partial x_i}\right)^2 + \frac{1}{2} \left(\frac{\partial \langle U_i \rangle}{\partial x_j} + \frac{\partial \langle U_j \rangle}{\partial x_i}\right)^2 + \left(\frac{\partial \langle U_j \rangle}{\partial x_j}\right)^2}, \quad (9)$$

where C_S is a constant to be chosen in the interval of 0.25–1.0 (Canuto and Cheng, 1997).

Some stability issues can arise when using the velocities from the previous time step and the eddy viscosity coefficient becomes large. So, the coefficient must fulfill the criterion

$$\frac{\nu_T \Delta t}{\Delta x_1 \Delta x_2} \leq \frac{1}{2}. \quad (10)$$

In two-equation models, U^* and l^* for Eq. (7) are related to transport equations, like the most widely used $k - \varepsilon$ turbulence closures model suggested by Launder and Sharma (1974):

$$\nu_T = C_\mu \frac{k_T^2}{\varepsilon}, \quad (11)$$

where $C_\mu = 0.09$ is known as the constant of proportionality, defined empirically through consideration of the flow under local equilibrium conditions, which states that at high Reynolds number, the rates of production and dissipation are of similar order of magnitude. Turbulent kinetic energy k_T is taken according to Eq. (6) and turbulence dissipation rate:

$$\varepsilon = \frac{C_\mu^{3/4} k_T^{3/2}}{L}, \quad (12)$$

where L is the turbulence length scale. Then turbulent kinetic energy and turbulence dissipation rate, eddy viscosity can be determined by the one equation turbulence model.

3.2. Numerical model

In the present study, the turbulence in the wave breaking process is treated by using artificial viscosity and interpolating kernel (Violeau and Rogers, 2016) and an empirical equation of compressibility by Batchelor (1967). Under these empirical considerations and some modification of the numerical model of empirical constants, the computational stability can be established with a reasonably small artificial viscosity coefficient α (see Eq. (13)). Interaction between the particles on the boundary is described by the Lennard-Jones potential and fluid particle trajectories are determined using the Verlet method for 2D motion. According to De Padova et al. (2009), in the limits where the kernel smoothing length and the interparticle spacing become small, the kernel is assumed to have compact support and to some extent, there seems to be no difference which kernel is used as long as basic requirements are met. However, in practice, values are not small and choice of kernel can drastically change the computational results (Rosswog, 2015). The fundamentals of the modified SPH method for free surface motion were described by Monaghan (1992, 1994, 2000).

In the SPH model, the artificial viscosity for a fluid is defined as

$$\nu_{A,ij} = \frac{-\alpha \mu_{ij} \bar{c}_{ij}}{\bar{\rho}_{ij}}, \quad (13)$$

where the following velocity dependent variable is

$$\mu_{ij} = \frac{h(\mathbf{v}_i - \mathbf{v}_j) \cdot (\mathbf{x}_i - \mathbf{x}_j)}{(\mathbf{x}_i - \mathbf{x}_j)^2 + (0.01h^2)}. \quad (14)$$

The overbar is an averaging operator, i.e., $\bar{\rho}_{ij} = \frac{1}{2}(\rho_i + \rho_j)$ and ρ_i and ρ_j are the density at particles i and j , respectively; $\bar{c}_{ij} = \frac{1}{2}(c_i + c_j)$ and c_i and c_j are the sound speed at particles i and j , respectively; $h = 1.2\Delta x$ is the smoothing length, where $\Delta x (= \Delta x_1 = \Delta x_2)$ is the space step and α is a constant that depends on the particular type of simulation being run and requires careful numerical calibration.

The SPH eddy viscosity at a fixed point $i = a$ is determined as

$$\nu_{SPH} = \frac{-\alpha c \sum_j \mu_j W_{aj}}{\sum_j \rho_j W_{aj}}, \quad (15)$$

where averaged viscosity at a fixed point is $\mu_{average} = \sum_j \mu_j W_{aj}$ and averaged density of mass at a fixed point is $\rho_{average} = \sum_j \rho_j W_{aj}$. The density of each particle is $\rho_i = \sum_j m_j W_{ij}$, where the particle j mass is m_j and the interpolation kernel is W_{ij} .

4. RESULTS

The experimental and numerical results correspond to the wave and bottom boundary layer conditions. In the first subsection, the eddy viscosity is specified according to the modified mean velocity and its derivatives. In the second subsection, the artificial viscosity is determined by numerical modelling. In the last subsection, the experimentally evaluated theoretical and empirical formulae of eddy viscosity and the numerically determined eddy viscosity values are compared.

4.1. Experimental results' treatment

It should be pointed out that the assumption of a purely shear straining velocity field in the bottom and surface boundary layers, which allows use of Eq. (4), is not valid for all instants and flow areas in the shoaling region, where the flow results from the superposition of the incoming waves, surface breaking and reflected wave. In the Boussinesq-type models for surface waves, the flow is represented through a decomposition of the velocity into a potential and a rotational part (see Briganti et al., 2004). The direct ensemble averaged measured velocity solutions confirm that both, eddy viscosity formulae Eq. (4) and Eq. (5) can result in peaks and negative values. This is apparently due to the velocity corresponding to a potential part where its gradient components do not represent the shear straining. Thus, an irrotational flow may be removed from the measured velocity by specifically treating the mean velocity and its derivatives. The velocity corresponding to a rotational part may be gained by subtracting the velocity just outside the bottom boundary layer from the local velocity: $\langle \vec{U} \rangle_t = \langle \vec{U} \rangle - \langle \vec{U} \rangle_b$. Furthermore, mean velocity gradient components should be modified by the functions that depend on the distance above the bottom:

$$\begin{aligned} \left(\frac{\partial \langle U_1 \rangle}{\partial x_1} \right)_t &= \frac{\partial \langle U_1 \rangle}{\partial x_1} - A(x_2), & \left(\frac{\partial \langle U_2 \rangle}{\partial x_2} \right)_t &= \frac{\partial \langle U_2 \rangle}{\partial x_2} - B(x_2), & \left(\frac{\partial \langle U_1 \rangle}{\partial x_2} \right)_t &= \frac{\partial \langle U_1 \rangle}{\partial x_2} - C(x_2), \\ \left(\frac{\partial \langle U_2 \rangle}{\partial x_1} \right)_t &= \frac{\partial \langle U_2 \rangle}{\partial x_1} - D(x_2). \end{aligned}$$

The weak compressibility of the fluid considered in Eq. (5) is based on the experimental observations showing that on the wave motion in the surf zone, a substantial amount of air is mixed into the water due to the surface breaking. It should be noted that for a two-dimensional flow, which corresponds to the experimental results, the non-zero divergence of the mean velocity is found, i.e.

$\frac{\partial \langle U_1 \rangle}{\partial x_1} + \frac{\partial \langle U_2 \rangle}{\partial x_2} \neq 0$, and a vertical velocity gradient component is negligible, i.e. $\frac{\partial \langle U_3 \rangle}{\partial x_3} \approx 0$, and can be ignored in Eq. (5).

4.2. Numerical model set-up

Numerical experiments were performed with the modified SPH model to simulate the wave breaking on the sloping bottom. Several modifications were introduced to the model setup. The numerical model domain was divided into two sections: 1) sloping bottom part and 2) horizontal bottom part. The sloping bottom 1:17 section was considered to be the same as in the physical model. The horizontal bottom between the reference point and the wave generator (Fig. 1) is considerably shortened. The reason is that a reduced number of particles per fluid volume allows speed-up of the numerical integration. The additional vertical extension in the sloping bottom end of the wave flume was used to keep the number of particles constant. However, to avoid particles' loss due to overtopping from 2D geometrical boundaries, the special criterion in the open-code SPH model was included to detect particles overtopped and move them back to the computational domain.

The wave generator used in the numerical model produced free surface crests motion. This motion becomes apparent in the wave flume after vanishing of the system self-oscillations. The length of the surface waves is around 4 m and directly observed phase speed in the horizontal bottom part of the numerical model domain is approximately 1.75 m s^{-1} (cf. experimentally observed wave celerity in Table 1). It is assumed that the speed of sound in Eq. (13) is constant, i.e. $\bar{c}_{ij} = 1440 \text{ m s}^{-1}$. The wave absorbing in the sloping bottom has a frequency of 0.5 Hz. The different phases, i.e. forward and backward position of the fluttering plate of the flap-type generator in the surface wave production, are shown in Figs 2a and 2b, respectively. In the wave generator mode, the breaking of particles formed free surface is in clear evidence. Regardless of a comparatively small number of particles, the wave production in the horizontal bottom and wave breaking along the sloping bottom is qualitatively in a good agreement with the experimental observations of the surface boundary layer.

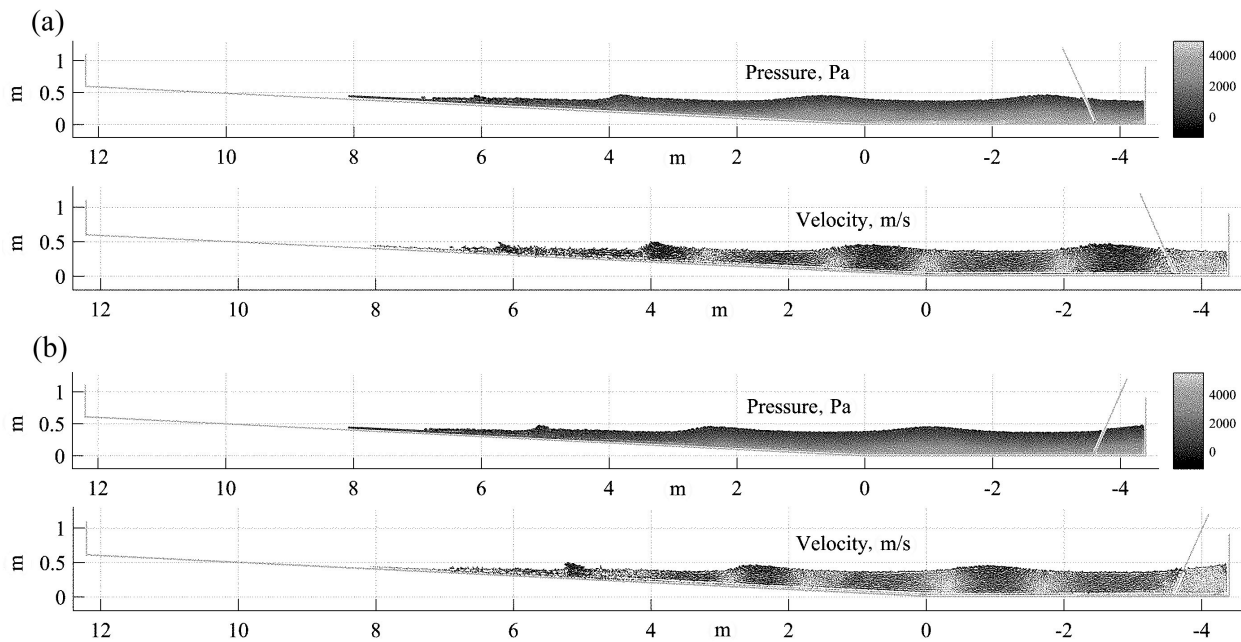


Fig. 2. SPH simulations of surface waves using an oscillating plate in: a) upper sub-plot shows the pressure and lower sub-plot shows the velocity at the time instant after 106.5 s; b) upper sub-plot shows the pressure and lower sub-plot shows the velocity at the time instant after 107.5 s.

In our implementation, the parallel computations were not used and therefore 1 s of simulation (consisting 1500 calculation steps) took around 25 min of real time in the used laptop with Intel® Core™ i7-8650U Processor. The structure of the SPH method is very suitable for parallelizing the computational process between the cores, on a cluster of computers or on a GPU (Ihmsen et al., 2011).

4.3. Comparison of experimental and numerical findings

Wave patterns are characterized by mean free surface displacement within the wave period (Fig. 3) along the chosen profiles (see Table 2), normalized by the local time average water depth. According to Fig. 3, wave breaking appears from 0.7–0.9 of the dimensionless wave period. Profile 16 is positioned in deeper water as compared to the position of profile 17, which is positioned in deeper water than the position of profile 18 on the slope.

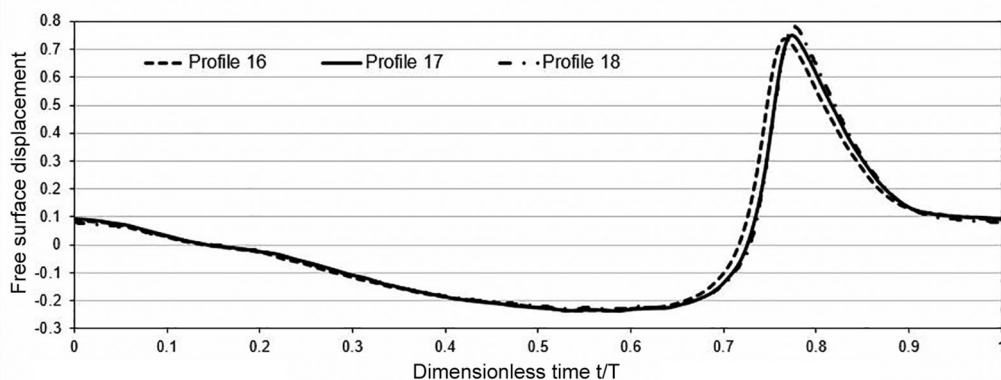


Fig. 3. The mean free surface displacement for three profiles. The profile numbers correspond to the location of measuring profiles 16, 17 and 18 in Table 2.

Measured turbulent kinetic energy according to Eq. (6) (see Fig. 4) was calculated at five different heights at one profile: a) 0.067 m; b) 0.052 m; c) 0.040 m; d) 0.028 m; and e) 0.006 m on sloping bottom. Turbulent kinetic energy demonstrates two local maximums: at instants when the surface roller is passing measurement profile 17, i.e. dimensionless wave period 0.65–0.75, and directly after the wave crest, i.e. dimensionless wave period 0.80–0.85. After breaking of a wave, there is a local minimum in the turbulent kinetic energy value occurring during a dimensionless wave period 0.00–0.10, which then converges to more or less constant value during a dimensionless wave period 0.10–0.60. It can be seen that the turbulent kinetic energy varies almost linearly with the increasing height from the bed.

The eddy viscosity was determined at the height of 0.028 m above bottom. Using the modified velocity gradient components, the solution resulting from the non-diagonal elements from the Reynolds stress tensor in Eq. (4) is shown by a dash-dot curve in Fig. 5. It can be seen that the eddy viscosity shows one distinct local maximum at instances when the surface roller is passing measurement profile 17, occurring at the dimensionless wave period 0.80. Eddy viscosity based on the first and second diagonal elements from the Reynolds stress tensor in Eq. (5) is shown as curves with shorter and longer dashed, respectively in Fig. 5. As can be seen, eddy viscosity shows two local maximums, similar to the turbulent kinetic energy in Fig. 4. However, the second diagonal elements correspond to significantly lower values. Also, Fig. 5 shows averaged eddy viscosity values, derived from the results of Eq. (4) and Eq. (5) (shown as a continuous curve).

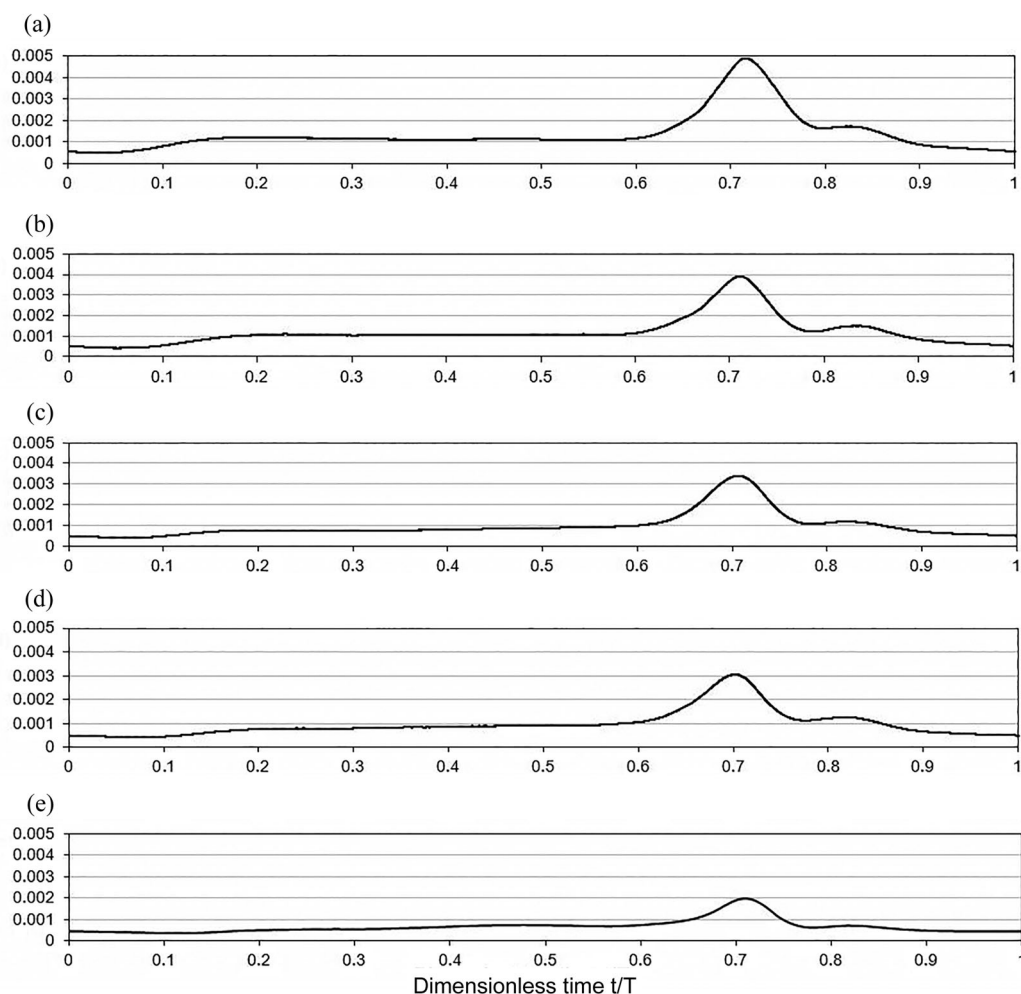


Fig. 4. Measured turbulent kinetic energy at different heights above sloping bottom: a) 0.067 m; b) 0.052 m; c) 0.040 m; d) 0.028 m and e) 0.006 m.

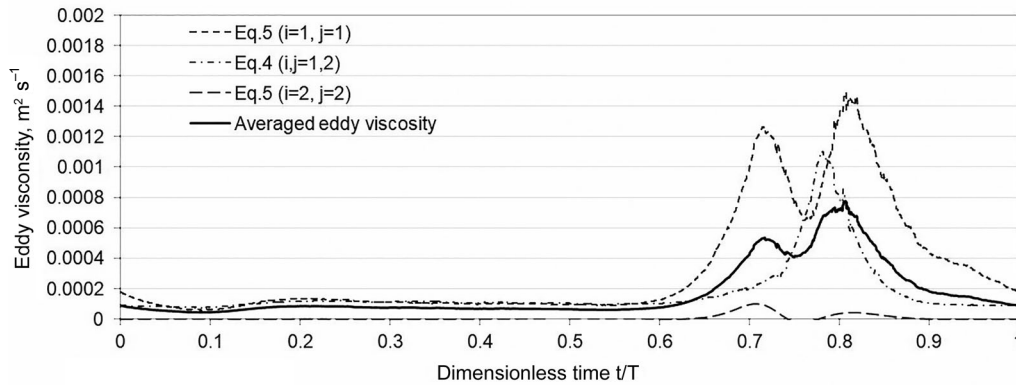


Fig. 5. Eddy viscosity based on theoretical equations with the surface direction index i and the flow direction index j . The averaged eddy viscosity values, derived from the results of Eq. (4) and Eq. (5), are shown as a continuous curve.

The averaged eddy viscosity presented in Fig. 5 is compared with the empirical and numerical modelling results in Fig. 6. The figure shows that the first local maximum of the averaged eddy viscosity corresponds to the $k - \epsilon$ model eddy viscosity predictions by Eq. (11) (short dashed curve in Fig. 5), i.e. it occurs during the dimensionless wave period 0.65–0.75. Further, the second local maximum of the averaged eddy viscosity corresponds to the Smagorinsky model eddy viscosity mixing length model, Eq. (9) (dash-dot curve in Fig. 6), it occurs during the dimensionless wave period 0.75–0.85. However, neither of the local maximums of the empirical models is in full correlation with the averaged eddy viscosity maximum. Furthermore, empirical models have lower values during the entire wave period than the averaged eddy viscosity. Inside the wave trough, all three eddy viscosities show more or less constant values. However, the eddy viscosity values of the Smagorinsky model correspond better to the averaged eddy viscosity, and the $k - \epsilon$ model eddy viscosity shows twice higher values.

Uniform eddy viscosity based on the mixing length model in Eq. (8) (long dashed curve in Fig. 6) shows a constant value of $5.4 \times 10^{-4} \text{ m}^2 \text{ s}^{-1}$. This value is higher than most of previous eddy viscosity results, except on averaged eddy viscosity second local maximum.

According to the numerically determined SPH eddy viscosity in Eq. (15) (dotted curve in Fig. 6), its local maximum is directly under the surface roller. However, within an entire wave period, SPH eddy viscosity gives higher values than the uniform eddy viscosity.

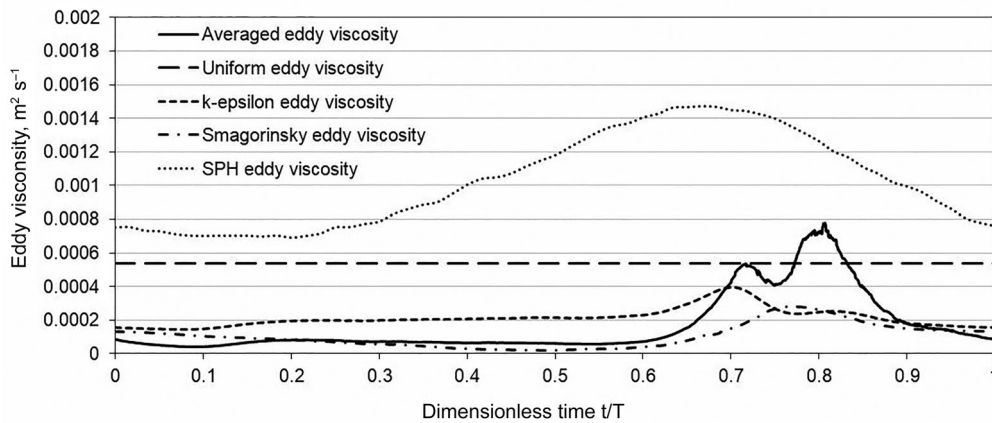


Fig. 6. Eddy viscosity estimates from different approximations: theoretical (averaged eddy viscosity in Fig. 5), empirical (uniform, $k - \epsilon$ and Smagorinsky eddy viscosity) and numerical (SPH eddy viscosity) predictions.

5. DISCUSSION

The eddy viscosity values were estimated according to formulae Eq. (4) and Eq. (5), which represent certain relationships between the velocity fluctuations correlation coefficients, turbulence kinetic energy and mean velocity gradient components. It was found that the ensemble averaged measured velocity predicted eddy viscosity is associated with peaks and negative values (see Oldekop et al., 2015), which are absent in the broadly accepted empirical predictions. Spurious peaks and negative values are apparently related to the velocity corresponding to a potential part of the flow where its gradient components do not represent the shear straining and manifest themselves when the shear stress and the velocity gradient change signs, i.e. flow reversal. This phenomenon has been reported by Perrier et al. (1995), Davies and Villaret (1999) and Malarkey and Davies (2004). We followed the methodology proposed by Briganti et al. (2004), where the flow is represented through a decomposition of the velocity into a potential and a rotational part. A possible alternative to solve the eddy viscosity problem was suggested by Shih et al. (1996), which was based on the relation between the Reynolds stress tensor and the strain rate of the mean flow through the nonlinear Reynolds stress model.

In this paper, the approach presented by Briganti et al. (2004), was tested by using the formulae Eq. (4) and Eq. (5), where the mean velocity and its derivatives were specifically treated. The irrotational flow was removed from the measured velocity by removing the oscillating part of the flow from the mean velocity and modifying its derivatives fields by the depth-dependent and time independent constants. The velocity corresponding to a rotational part was obtained by subtracting the velocity just outside the bottom boundary layer from the local velocity, and the mean velocity gradient components were modified by functions $A(x_2)$, $B(x_2)$, $C(x_2)$, $D(x_2)$, which depend on the distance from the bottom. Apparently, this specific treatment of the mean velocity and its derivatives is a possible source of some errors, which is not important in respect of qualitative results. In our approach, the used functions follow some conditions, i.e. $A(x_2) \ll B(x_2)$ and $C(x_2) = D(x_2)$. The latter indicates that the specific correction functions correspond to the irrotational flow of the velocity field. In other words, according to the approach by Briganti et al. (2004), the rotational velocity can be expressed as

$$\overline{\langle U \rangle}_p = \overline{\langle U \rangle}_b + a x_2 \hat{a} + b x_2^2 \hat{b}, \quad (16)$$

where coefficients $a = f_a(A, B, C, D)$, $b = f_b(A, B, C, D)$ and unit vectors are \hat{a} and \hat{b} .

In the surf zone, the surface wave undergoes changes due to the velocity shear near bottom and free surface non-linear deformation, the turbulence is generated from two sources: bottom boundary layer and surface boundary layer. Also, the present study takes into account that the eddy viscosity is not related to the tube flow oscillation approximation, where it is sufficient to use the relationship between the correlation coefficient of cross flow directional fluctuations and the vertical component of the along channel velocity gradient. Furthermore, a substantial amount of air that is captured within the wave motion due to breaking, results in the non-zero divergence of the mean velocity. This indicates that the air mixing in the water of the plunging breaker corresponds to a weakly compressible fluid.

Considering variations in the turbulent kinetic energy values during the wave period and over the water column, it is apparent from Eq. (5) that the eddy viscosity values are also changing over time and space. Regarding the new experimental findings, it could be suggested that using the coastal engineering models, the empirical and numerical predictions should follow the theoretical eddy viscosity time and space dependent functions in the surf zone. It should be taken into account that the turbulence is generated both in the surface and bottom boundary layers, which merge in the surf zone. Therefore, empirical predictions are unable to forecast the eddy viscosity values during the wave period and over the water column with acceptable accuracy.

6. CONCLUSIONS

To clarify the complex turbulence dynamics of breaking waves in the surf zone, this study revisited a data set derived from a relevant experiment. The empirical and numerical predictions of eddy viscosity were

compared to the experimental findings obtained from the physical beach model presented by Liiv (2007). The theoretically predicted eddy viscosity was derived from the combined functions of Reynolds stresses, modified mean velocity and its gradient components and from turbulent kinetic energy for weakly compressible fluid. The irrotational flow that masked the turbulence velocity field under a breaking wave was removed by means of oscillating velocity at bottom and four coefficients were used to modify the particular mean velocity gradient components. The instantaneous eddy viscosity coefficient is positively valued during the wave period, which gives evidence of the modified velocity field corresponding well to the shear and compression strain that results from the bottom and surface boundary layers. It was found that the eddy viscosity determined experimentally is of high complexity under a breaking wave on the sloping bottom than predictions of the empirical formulae. Also, it is required to improve the meshless numerical modelling to determine the artificial viscosity and the corresponding eddy viscosity more accurately by a number of particles “smeared” in space. It is demonstrated that the theoretically determined eddy viscosity values are in the same order of magnitude as the empirical and numerical predictions, and follow reasonably well the production of turbulence during wave breaking.

It was found that the SPH eddy viscosity corresponds qualitatively well with the theoretical eddy viscosity determined from the combined functions of Reynolds stresses modified mean velocity and its gradient components and turbulent kinetic energy for compressible fluid. As a possible future task, SPH modelling approach should be used more comprehensively in dealing with the counterparts of coastal processes, e.g., stratified flow mixing, air-water interaction and sediments transport in the surf zone due to wave breaking. In the complex coastal environment, where waves and currents interact with bed forms, the stratified flow and wind wave numerical models should be used to predict bottom changes (cf. Laanearu et al., 2011).

ACKNOWLEDGEMENTS

The SPH model used herein was developed by the master-level student Gleb Bogomol during the special course of fluid dynamics at Tallinn University of Technology. This work was partly supported by the Estonian Ministry of Education and Research [grant IUT 19-17]. The publication costs of this article were covered by the Estonian Academy of Sciences.

REFERENCES

- Batchelor, G. K. 1967. *An Introduction to fluid dynamics*. Cambridge University Press, Cambridge, United Kingdom.
- Battjes, J. A. 1988. Surf-zone dynamics. *Annu. Rev. Fluid Mech.*, **20**, 257–291.
- Bertin, J. J., Periaux, J., and Ballmann, J. 1992. *Advances in Hypersonics. Modeling Hypersonic Flows. – Volume 2*. Birkhäuser, Boston, USA.
- Briganti, R., Musumeci, R. E., Bellotti, G., Brocchini, M., and Foti, E. 2004. Boussinesq modeling of breaking waves: description of turbulence. *J. Geophys. Res.*, **109**(C0701).
- Canuto, V. M. and Cheng, Y. 1997. Determination of the Smagorinsky-Lilly constant CS. *Phys. Fluids*, **9**, 1368.
- Capone, T., Panizzo, A., and Monaghan, J. J. 2010. SPH modelling of water waves generated by submarine landslides. *J. Hydraul. Res.*, **48**, 80–84.
- Chang, K.-A. and Liu, P. L.-F. 1999. Experimental investigation of turbulence generated by breaking waves in water of intermediate depth. *Phys. Fluids*, **11**, 3339–3400.
- Dalrymple, R. A. and Rogers, B. D. 2006. Numerical modelling of water waves with the SPH method. *Coastal Eng.*, **53**, 141–147.
- Davies, A. G. and Villaret, C. 1999. Eulerian drift induced by progressive waves above rippled and very rough beds. *J. Geophys. Res.*, **104**(C1), 1465–1488.
- De Padova, D., Dalrymple, R. A., Mossa, M., and Petrillo, A. F. 2009. SPH simulations of regular and irregular waves and their comparison with experimental data. *arXiv:0911.1872v1*
- Fredsøe, J. and Deigaard, R. 1992. *Mechanics of coastal sediment transport. Advanced Series on Ocean Engineering – Volume 3*. World Scientific Publishing, Singapore.
- Gomez-Gesteira, M., Rogers, B. D., Dalrymple, R. A., and Crespo, A. J. C. 2010. State-of-the-art of classical SPH for free-surface flows. *J. Hydraul. Res.*, **48**, 6–27.
- Ihmsen, M., Akinci, N., Becker, M., and Teschner, M. 2011. A parallel SPH implementation on multi-core CPUs. *Comput. Graphics Forum*, **30**(1), 99–112.
- Laanearu, J., Koppel, T., Soomere, T., and Davies, P. A. 2007. Joint influence of river stream, water level and wind waves on the height of sand bar in a river mouth. *Nord. Hydrol.*, **38**(3), 287–302.

- Laanearu, J., Vassiljev, A., and Davies, P. A. 2011. Hydraulic modelling of stratified bi-directional flow in a river mouth. In *Proceedings of the Institution of Civil Engineers: Engineering and Computational Mechanics*, **164**(4), 207–216.
- Lauder, B. E. and Sharma, B. I. 1974. Application of the energy-dissipation model of turbulence to the calculation of flow near a spinning disc. *Lett. Heat Mass Transfer*, **1**(2), 131–138.
- Lee, E. S., Violeau, D., Issa, R., and Ploix, S. 2010. Application of weakly compressible and truly incompressible SPH to 3-D water collapse in waterworks. *J. Hydraul. Res.*, **48**, 50–60.
- Liiv, T. 2007. An experimental investigation of the oscillatory boundary layer around the breaking point. *Proc. Est. Acad. Sci.*, **13**(3), 215–233.
- Liiv, T. and Lagema, P. 2008. The variation of the velocity and turbulent kinetic energy field in the wave in the vicinity of the breaking point. *Est. J. Eng.*, **14**(1), 42–64.
- Lundgren, H. and Sorensen, T. 1958. A pulsating water tunnel. In *Proceedings 6th Coastal Engineering Conference, ASCE*, 356–358.
- Madsen, O. S. and Grant, W. D. 1976. Quantitative description of sediment transport by waves. *Coastal Eng. Proc.*, **1**(15), 1093–1112.
- Malarkey, J. and Davies, A. G. 2004. An eddy viscosity formulation for oscillatory flow over vortex ripples. *J. Geophys. Res.*, **109**, C12016.
- Monaghan, J. J. 1992. Smoothed particle hydrodynamics. *Annu. Rev. Astron. Astrophys.*, **30**, 543–574.
- Monaghan, J. J. 1994. Simulating free surface flows with SPH. *J. Comput. Phys.*, **110**, 399–406.
- Monaghan, J. J. 2000. SPH without a Tensile Instability. *J. Comput. Phys.*, **159**, 290–311.
- Morris, J. P. 2000. Simulating surface tension with smoothed particle hydrodynamics. *Int. J. Numer. Methods Fluids*, **33**(3), 333–353.
- Oldekop, N. and Liiv, T. 2013. Measurement of the variation of shear velocity on bed during a wave cycle. *J. Earth Sci. Eng.*, **3**(5), 322–330.
- Oldekop, N., Liiv, T., and Lagema, P. 2015. The variation of turbulent eddy viscosity during a wave cycle. *E-Proceedings of the 36th IAHR World Congress, June 28–July 3, 2015, Hague, Netherlands*, 1–5.
- Peregrine, D. H. 1983. Breaking waves on beaches. *Annu. Rev. Fluid Mech.*, **15**, 149–178.
- Perrier, G., Villaret, C., Davies, A. G., and Hansen, E. A. 1995. Numerical modelling of the oscillatory boundary layer over ripples. *MAST G8-M Coastal Morphodynamics Project, Final Overall Meeting, Delft Hydraul., Gdansk, Poland*, 4.26–4.29.
- Rodi, W. 1980. *Turbulence models and their application in hydraulics – A state of the art review*. International Association for Hydraulic Research, Delft.
- Rogers, B. D., Dalrymple, R. A., and Stansby, P. K. 2010. Simulation of caisson breakwater movement using SPH. *J. Hydraul. Res.*, **48**, 135–141.
- Rosswog, S. 2015. SPH methods in the modelling of compact objects. *Living Rev. Comput. Astrophys.*, **1**(1).
- Shao, S. 2006. Simulation of breaking wave by SPH method coupled with $k - \epsilon$ model. *J. Hydraul. Res.*, **44**(3), 338–349.
- Shih, T.-H., Zhu, J., and Lumley, J. L. 1996. Calculation of wall-bounded complex flows and free shear flows. *Int. J. Numer. Methods Fluids*, **23**, 1133–1144.
- Svendsen, I. A. and Putrevu, V. 1996. Surf-zone hydrodynamics. *Adv. Coastal Ocean Eng.*, **2**, 1–78.
- Ting, F. C. K. and Kirby, J. T. 1994. Observation of undertow and turbulence in a laboratory surf zone. *Coastal Eng.*, **24**, 51–80.
- Ting, F. C. K. and Kirby, J. T. 1995. Dynamics of surf-zone turbulence in a strong plunging breaker. *Coastal Eng.*, **24**, 177–204.
- Ting, F. C. K. and Kirby, J. T. 1996. Dynamics of surf-zone turbulence in a spilling breaker. *Coastal Eng.*, **27**, 131–160.
- Violeau, D. and Rogers, B. D. 2016. Smoothed particle hydrodynamics (SPH) for free-surface flows: past, present and future. *J. Hydraul. Res.*, **54**(1), 1–26.

Turbulentse viskoossuse katseline uurimine lainerenni kaldpinnal murdlaine all ja võrdlused empiiriliste ning numbriliste arvutustulemustega

Nelly Oldekop, Toomas Liiv ja Janek Laanearu

On selgitatud turbulentsi parameetrite määramist sukelduva murdlaine all. Kiirusväli on mõõdetud lainerenni kaldpinnalisel põhjal Doppleri laseranemomeetriga. Kasutades Reynoldsi pinge anisotroopsust kokkusurumatu vedeliku jaoks, on leitud, et ansamblikeskmestatud mõõdetud kiirusega määratud turbulentsne viskoossus on seotud singulaarsustega, mis ei esine laialdaselt kasutatavate empiiriliste valemite arvutustulemustes. Seetõttu määratakse hetkeline turbulentsne viskoossustegur Reynoldsi pingete, matemaatiliselt täiendatud keskmise kiiruse ja selle gradientkomponentide ning turbulentsne kineetilise energia järgi. Modifitseeritud keskmine kiirus ja selle tuletised parandavad oluliselt turbulentsne viskoossusteguri arväärtusi laineperioodi jooksul, millest võib järeldada, et matemaatiliselt muudetud kiirusväli vastab hästi pöörisele keerisvälja tingimustele. Mõõtmistega saadud turbulentsne viskoossusteguri arväärtusi on võrreldud ka olemasolevate empiiriliste valemite arvutustulemustega, et näidata erinevate meetoditega saadud turbulentsne viskoossustegurite väärtusi laineperioodi jooksul. Nõrgalt kokkusurutava vedeliku hüdromehaanika numbrilist mudelit SPH on kasutatud kunstliku viskoossuse määramiseks laineperioodi jooksul. SPH turbulentsne viskoossusteguri arväärtusi on samuti võrreldud mõõtmistega saadud turbulentsne viskoossusteguri arvutustulemustega.